Four-band effective square-lattice model for Bernal-stacked bilayer graphene

Szu-Chao Chen (陳思超) [1], Alina Mreńca-Kolasińska [2,*] and Ming-Hao Liu (劉明豪) [3,†]

[1] *Department of Electro-Optical Engineering, National Formosa University, Yunlin, Taiwan*

[2] *AGH University, Faculty of Physics and Applied Computer Science, al. Mickiewicza 30, Krakow 30-059, Poland*

[3] *Department of Physics and Center of Quantum Frontiers of Research and Technology (QFort), National Cheng Kung University, Tainan 70101, Taiwan*

Recent experimental progress on Bernal-stacked bilayer graphene (BLG) has shown its versatility not only in exotic physics but also in practical applications in electronic devices thanks to its gate-tunable band gap. Modeling and simulating quantum transport experiments on BLG samples, however, has so far remained rather limited. Here we present a four-band effective square-lattice model and demonstrate its power and reliability by revisiting BLG transport experiments, including the classic magnetotransport of quantum Hall effect and transverse magnetic focusing, and more recent studies of anti-Klein to Klein tunneling and Aharonov-Bohm effect. Our model originates from discretizing the continuum model but does not suffer from the fermion doubling due to accidental mapping of both K and K' valleys from the original hexagonal Brillouin zone (BZ) to the square BZ of the effective model. Such a mapping is expected to exist in more two-dimensional materials of hexagonal lattices.

I. INTRODUCTION

Bilayer graphene (BLG) is a versatile platform for a variety of electronic devices. Recently, superconductivity has been demonstrated in magic angle twisted BLG [1] as well as Bernal-stacked BLG [2], while BLG-based moiré heterostructures have been evidenced to manifest unconventional ferroelectricity [3] and formation of the Wigner crystal [4]. The natural Bernal-stacked, also called AB-stacked BLG, thanks to its band gap controllable by displacement field, can be used as a base for electronic components like gate-defined quantum point contacts (QPCs) [5–9], quantum dots [8,10–13], cavities [14], and topological channels [15–17]. Exploiting the gate-tunable gap also led to the demonstration of transverse magnetic focusing of carriers between gate-defined QPCs [18], and fully gate-controlled interferometers [19,20].

Theoretical modeling of quantum transport is commonly based on the atomistic tight-binding model (TBM). Modeling realistic Bernal-stacked BLG devices, of size of the order of hundreds of nanometers, is highly demanding. Faithful reproduction of experimental results was limited to rather simple geometries with lateral translational invariance [21,22]. The scalable model [23], particularly useful for single-layer graphene, introduces a scaling factor s_f that may reduce the computational burden. However, for AB-stacked BLG the scaling factor is rather limited due to the interlayer coupling, making simulations for more complex devices challenging. Another approach is solving the Dirac equation within the continuum model, however, discretizing it may produce spurious solutions due to the fermion doubling. Circumventing this problem has been carried out by adding an extra dimension to the computational lattice [24] or by various discretization schemes [25–30]. Many adaptations for condensed-matter physics, and in particular graphene, have been developed [31–35], which in certain cases can also be extended to Bernal-stacked BLG [36].

In this work, we show a discretization scheme of the continuum model, which can capture transport properties of Bernal-stacked BLG. The resulting four-band effective square-lattice model [see Fig. 1(a) and the rest of the panels for an overview] can tackle large, realistic devices because of the greatly reduced computational burden. In the discretization scheme derived for the K valley, the fermion-doubled states show the properties of the K and K' valleys, and thus we need not remove them from the spectrum with the methods developed before [36] since they are beneficial for simulating phenomena involving both valleys. We demonstrate the advantage of this approach by revisiting recent experiments in BLG: integer quantum Hall effect [37,38], transverse magnetic focusing [39], Aharonov-Bohm effect in a gate-defined quantum ring [19], and Klein tunneling in bipolar junctions [22].

---

*Contact author: alina.mrenca@fis.agh.edu.pl

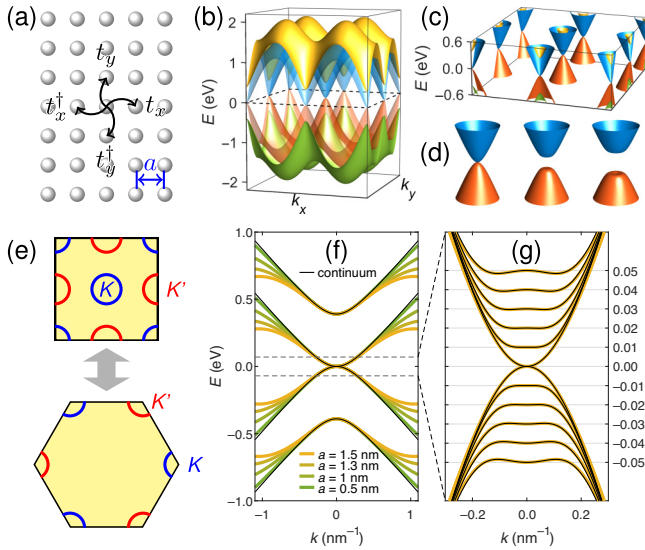†Contact author: minghao.liu@phys.ncku.edu.tw

FIG. 1. (a) The effective square-lattice model. (b) Band structure obtained from the effective model. (c) Close ups of the bands in (b) at low energy. (d) Band structure around $(k_x, k_y) = (0, 0)$ with $U = 0, 0.1, 0.2$ eV. (e) Schematic diagram showing the mapping between the hexagonal and square-lattice BZ with the K (K') valley marked by blue (red). (f) Line cuts of the bands at $U = 0$, with increasing square-lattice spacing a, compared to the continuum model (black curves). (g) The close up marked in (f) with $a = 1.5$ nm and U varying from 0 to 0.1 eV. Black curves are from the continuum model.

II. THE FOUR-BAND EFFECTIVE MODEL

In the widely adopted four-orbital continuum model for BLG, the Hamiltonian written in the basis of the orbitals on sites $A1$, $B1$, $B2$, $A2$, with the lower (upper) layer labeled by 1 (2), reads [40]

$$
\begin{pmatrix}
V + U/2 & v_F\pi^+ & \gamma_1 & 0 \\
v_F\pi^- & V + U/2 & 0 & 0 \\
\gamma_1 & 0 & V - U/2 & v_F\pi^- \\
0 & 0 & v_F\pi^+ & V - U/2
\end{pmatrix}, \quad (1)
$$

where v_F is the Fermi velocity of graphene, U is the asymmetry parameter arising from the symmetry breaking of the two graphene layers, V is the band offset, γ_1 is the hopping integral between pairs of orbitals on the dimer sites $B1$ and $A2$, $\pi^\pm = \xi p_x \pm i p_y$, and $\xi = \pm$ for the $\frac{K}{K'}$ valley. The dis-

cretization of the Hamiltonian on an artificial square lattice with four orbitals on each site ($A1$, $B1$, $B2$, $A2$) is done by replacing the spatial derivative in the momentum operators by the central finite-difference quotients for the spatial derivative (for a pedagogical explanation, see Ref. [41]). Upon this procedure, we obtain an effective Hamiltonian given by

$$
\mathcal{H} = \sum_n c_n^\dagger \mathbb{U}_n c_n + \sum_{\langle m,n \rangle} c_m^\dagger \mathbb{T}_{m \leftarrow n} c_n, \quad (2)
$$

where $c_n^\dagger$ (c_n) creates (annihilates) an electron on a square-lattice site labeled by n and located at $\mathbf{r}_n = (x_n, y_n)$, the second sum runs over all site pairs $\langle m, n \rangle$ that are nearest to each other, the onsite energy matrix is given by

$$
\mathbb{U}_n = \begin{pmatrix}
V_n + U_n/2 & 0 & \gamma_1 & 0 \\
0 & V_n + U_n/2 & 0 & 0 \\
\gamma_1 & 0 & V_n - U_n/2 & 0 \\
0 & 0 & 0 & V_n - U_n/2
\end{pmatrix}, \quad (3)
$$

where U_n and V_n generalized from those in Eq. (1) are, respectively, the asymmetry parameter and band offset on site n, and the hopping matrix $\mathbb{T}_{m \leftarrow n}$ is depicted in Fig. 1(a) with

$$
t_x = \frac{t}{2}\begin{pmatrix}
0 & -i & 0 & 0 \\
-i & 0 & 0 & 0 \\
0 & 0 & 0 & -i \\
0 & 0 & -i & 0
\end{pmatrix} \quad \text{and}
$$

$$
t_y = \frac{t}{2}\begin{pmatrix}
0 & 1 & 0 & 0 \\
-1 & 0 & 0 & 0 \\
0 & 0 & 0 & -1 \\
0 & 0 & 1 & 0
\end{pmatrix}, \quad (4)
$$

where the hopping parameter is given by $t = \hbar v_F / a$ and the lattice spacing a is tunable within a reasonable range depending on the energy of interest.

III. BULK ENERGY BANDS

For an infinitely extending square lattice described by Hamiltonian (2) with translational invariance of $U_n = U$ and $V_n = 0$, we obtain the bulk BLG band structure

$$
E_{\mu,\nu} = \mu\sqrt{t^2(\sin^2 k_x a + \sin^2 k_y a) + \frac{U^2}{4} + \frac{\gamma_1^2}{2} + \nu\frac{1}{2}\sqrt{\gamma_1^4 + 4t^2(\sin^2 k_x a + \sin^2 k_y a)(U^2 + \gamma_1^2)}}, \quad (5)
$$

where $\mu, \nu = \pm 1$ are branch indices; see Appendix A. The four energy bands obtained from this model for $U = 0$ are presented in Fig. 1(b). One can see that in the first Brillouin zone (BZ), the Dirac cone is copied to $\mathbf{k} = (k_x, k_y) = (\sigma, \sigma')\pi/a$ with $\sigma, \sigma' = -1, 0, 1$ [Fig. 1(c)]. The low energy band structure considering a single cone with $U = 0, 0.1, 0.2$ eV is shown in Fig. 1(d).

By performing low-k expansions around the nine **k** points mentioned above (Appendix B), the nine cones in the square BZ of the effective model are found to correspond to the two nonequivalent valleys K and K' on the six corner points of the hexagonal BZ from the atomistic TBM; see Fig. 1(e). Specifically, the K valleys are mapped to $(\sigma, \sigma') = (0,0), (\pm 1, \pm 1), (\pm 1, \mp 1)$, while K' valleys to $(\sigma, \sigma') = (\pm 1, 0), (0, \pm 1)$. Thus the effective model, although obtained by discretizing the continuum model for the K valley, precisely captures the properties of both K and K' valleys. Bearing this in mind, division of the total conductance by 2 when performing transport simulations is sufficient to correct this doubling.

IV. SCALABILITY

Figure 1(f) compares the band structure given by the analytical formula from the continuum model and that from the effective model by Eq. (5) around **k** = 0, considering $U = 0$ and various lattice spacing a. Good agreement can be clearly seen at low energy. Upon increasing a, Eq. (5) based on the effective model starts to deviate from the exact band structure at lower k. The good agreement at low energy remains satisfactory even when $U \neq 0$. A few examples considering $a = 1.5$ nm and various U are shown in Fig. 1(g). The model catches the characteristic "Mexican hat" structure and is accurate close to the band edge even at the asymmetry parameter reaching $U = 0.1$ eV. Moreover, Eq. (5) is to a good approximation isotropic at low energy. This property is used for the calculation of the band offset for the transport calculations (see Appendix C).

V. NANORIBBONS

Having discussed the bulk spectrum of BLG, next we show that our effective model applies equally well to finite-width BLG ribbons, without and with the applied magnetic field B perpendicular to the graphene plane. In Figs. 2(a)–2(e), we consider a nanoribbon of width $W \approx 200$ nm [middle panel in Fig. 2(e)]. The enlargement of the structure used in the atomistic tight-binding (effective) model calculation is shown in the upper (lower) panel of Fig. 2(e). Band structures of the 200-nm ribbon at $B = 0$ calculated within the unscaled lattice model ($s_f = 1$) and its scaled variant with $s_f = 4$ are presented in Fig. 2(a), showing rather good consistency, especially the lowest few subbands (inset thereon). The consistency is even better at finite magnetic field as shown in Fig. 2(b) with $B = 5$ T. The counterparts of Fig. 2(a) with $B = 0$ and Fig. 2(b) with $B = 5$ T using the effective model are shown in Figs. 2(c) and 2(d), respectively, showing highly consistent features, including the eightfold degeneracy of the lowest Landau level, characteristic of the Bernal-stacked BLG, to be revealed in the following transport simulation.
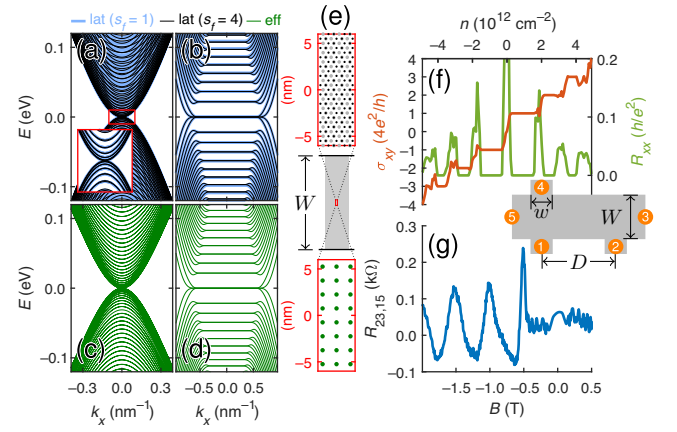

FIG. 2. Band structures of a BLG nanoribbon of width $W \approx 200$ nm, calculated using (a),(b) the atomistic TBM and (c),(d) the effective model, considering $B = 0$ in (a),(c) and $B = 5$ T in (b),(d). The structure of the considered ribbon is sketched in (e), where the upper and lower panels show the lattice structure of the atomistic TBM and effective model, respectively. (f) Longitudinal resistance R_{xx} and Hall conductivity σ_{xy} as a function of the carrier density n at $B = 14$ T calculated with grid spacing $a = 1$ nm. (g) Nonlocal resistance $R_{23,15}$ as a function of B at $n = -2.8 \times 10^{12}$ cm^{-2}. Inset between (f),(g): schematics of the system for the multiterminal transport calculations of (f),(g).

VI. CLASSIC MAGNETOTRANSPORT

Two classic magnetotransport experiments are revisited in the following: transverse magnetic focusing (TMF) [39] at moderate B, and integer quantum Hall effect [37] at strong B. Such multiterminal magnetotransport simulations require the gauge transformation for the chosen vector potential [42] as recently described in Ref. [43]. Generally, we consider the four-probe resistance $R_{ij,kl}$ with current flowing between i and j probes, and voltage between k and l probes. As shown by the inset between Figs. 2(f) and 2(g), we used a five-terminal geometry with leads labeled by $1, 2, \ldots, 5$ for both simulations. The dimensions of the probe width w, channel width W, and probe spacing D vary for the two cases and will be specified.

Figure 2(f) shows the Hall conductivity σ_{xy}, corresponding to the inset of Fig. 4 of Ref. [37], and the longitudinal resistance $R_{xx} = R_{53,12}$ at $B = 14$ T, considering $(w, W, D) = (199, 268, 401)$ nm and $a = 1$ nm for the effective model. To induce the Landau-level broadening, in the scattering region we add a random onsite potential with a uniform distribution within the range ± 0.1 eV. The calculated σ_{xy} shows plateaus quantized at $\pm(4e^2/h)N$, $N = 1, 2, \ldots$, with R_{xx} assuming nonzero value in between the plateaus and zero otherwise. Within the presented density range, up to the fourth plateau develops, in agreement with the experiment [37]. At high density, the model starts to show small discrepancy, namely doubling of the R_{xx}

peaks as a result of the subbands protruding below the flat subbands in the band structure [Fig. 2(d)]. For the TMF calculation, we consider a clean system with $(w, W, D) = (100.5, 567, 774)$ nm and $a = 1.5$ nm. Figure 2(g) shows the nonlocal resistance $R_{23,15}$ calculated at $n = -2.8 \times 10^{12}$ cm^{-2}, as a function of magnetic field, corresponding to Fig. 4(b) of Ref. [39]. We observe peaks of nonlocal resistance roughly at multiples of $B_1 \approx 0.5$ T, in good agreement with Ref. [39], and corresponding to cyclotron radius $R_c = \hbar\sqrt{\pi n}/eB_1 \approx 390$ nm. To sum up, we demonstrated that the model works well for realistic large-scale systems.

VII. THE AHARONOV-BOHM EFFECT

Quantum rings represent the most basic realization of the Aharonov-Bohm two-slit experiment [44] in solids. The magnetic flux piercing the area encircled by the two arms of the ring traversed by electrons introduces phase difference, which leads to conductance oscillation with the period of magnetic flux quantum $\phi_0 = h/e$. A number of works addressed this effect in quantum rings etched in graphene both theoretically [45–47] and experimentally [48–52]. Inevitable consequences of their fabrication are edge roughness, disorder, and impurities, which reduce the mean free path and coherence length. A better quality can be reached in interferometers relying on electrostatic confinement [53–55], which naturally leads to the proposal of defining Aharonov-Bohm rings by inducing an energy gap in gated BLG [19] revisited below.

The system studied here is sketched in Fig. 3(a), where the BLG sample (black) is encapsulated by hexagonal boron nitride (h-BN) layers (blue) of thickness $d_b = 45.1$ nm for the bottom and $d_t = 37.3$ nm for the top. The h-BN/BLG/h-BN sandwich is placed on a global back gate (dark gray), which tunes the band offset and asymmetry parameter together with the ring-shaped gate (orange) and the top gate (yellow semitransparent), separated from each other by a layer of aluminum oxide (white semitransparent). The back gate capacitance is obtained from the parallel-plate capacitor model as $C_{BG}/e = \varepsilon_0\varepsilon_{h\text{-}BN}/ed_b \approx 4.044 \times 10^{11}$ cm^{-2} V^{-1}, where ε_0 is the vacuum permittivity, $-e$ is the electron charge, and $\varepsilon_{h\text{-}BN} = 3.3$ is adopted. To qualitatively describe the nonuniform gate capacitances, we use model functions (see Appendix D) $C_{ring}(x,y)$ for the ring gate and $C_{TG}(x,y)$ for the top gate, as shown in Figs. 3(b) and 3(c), respectively. The spatially resolved carrier density induced by the gates is given, assuming no intrinsic doping, by $n(x,y) = [C_{BG}V_{BG} + C_{ring}(x,y)V_{ring} + C_{TG}(x,y)V_{TG}]/e$. From the band structure, Eq. (5) of the effective model, given the asymmetry parameter U and the carrier density n, we get the band offset V (Appendix C).
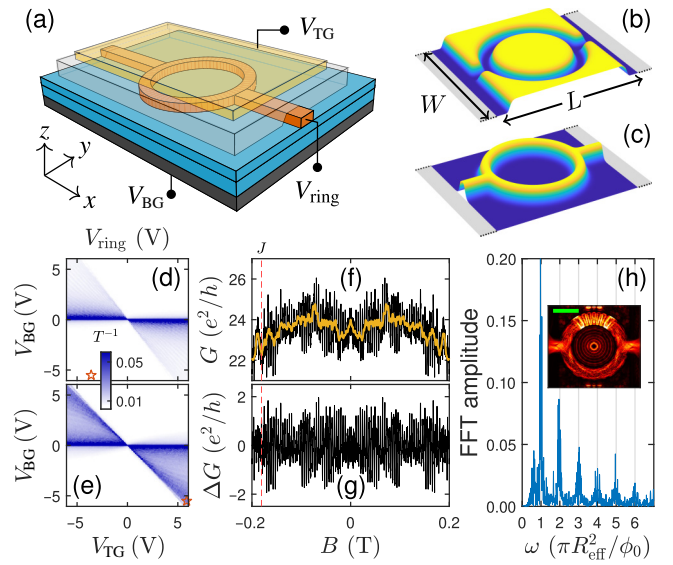

FIG. 3. (a) Schematics of the modeled device for studying the Aharonov-Bohm effect. Profiles of the capacitance functions modeling (b) the top gate and (c) the ring gate. Inverse transmission maps of $T^{-1}(V_{ring}, V_{BG})$ with $V_{TG} = 0$ and (e) $T^{-1}(V_{TG}, V_{BG})$ with $V_{ring} = 0$. (f) Conductance (black curve) as a function of B at the gate voltages marked by the stars in (d),(e) and its smoothed background (orange curve). (g) Oscillatory part ΔG and (h) its FFT. Inset in (h), an exemplary current density profile J (dark or bright means low or high values) corresponding to the red dashed line in (f),(g). Scale bar: 500 nm.

The triply gated BLG described by our effective model as a $L = 1800$ nm long and $W = 1599$ nm wide square lattice of spacing $a = 1.5$ nm, attached to two leads [gray patches in Figs. 3(b) and 3(c)]. Basic characterization transport simulations (for details see Appendix D) for the two-terminal inverse transmission T^{-1} (in order for a better comparison with the resistance measurement [19]) are shown in Fig. 3(d) for $T^{-1}(V_{ring}, V_{BG})$ with $V_{TG} = 0$ and in Fig. 3(e) for $T^{-1}(V_{TG}, V_{BG})$ with $V_{ring} = 0$, showing good agreement with the experiment [compare to Fig. 1(b) in Ref. [19]]. To reproduce the experimentally observed Aharonov-Bohm effect, we focus on gate voltages $(V_{BG}, V_{TG}, V_{ring}) \approx (-5.52, 5.88, -3.6)$ V [marked by stars in Figs. 3(d) and 3(e)] with which the region outside the ring is "pinched off." Example current density is shown in the inset of Fig. 3(h), confirming the current is mainly circulating in the ring. For the nominal dimensions of the ring, with $R_{in} = 500$ nm and $R_{out} = 580$ nm being the inner and outer radius of the ring, respectively, we expect the Aharonov-Bohm oscillation period to be within the range $2\hbar/eR_{out}^2 = 3.9$ mT to $2\hbar/eR_{in}^2 = 5.26$ mT. The following Figs. 3(f) and 3(g) correspond to Fig. 1(c) of Ref. [19], and Figs. 3(h) to 1(d) therein. Figure 3(f) shows the conductance calculated for magnetic

field between ±200 mT (black line), while the fluctuating orange line is the smooth background. The background is obtained by smoothing the curve with Savitzky-Golay filter, using a window size 7.5 mT and polynomial order 2. It is then subtracted from the original curve to show the oscillatory part of the conductance ΔG in Fig. 3(g). By performing fast Fourier transform (FFT) of ΔG, we obtain the spectrum shown in Fig. 3(h), where the frequency axis is presented in the units of $\pi R_{\text{eff}}/\phi_0$, and R_{eff} is the effective radius of the ring. The FFT spectrum contains a set of peaks falling at $\upsilon \times \pi R_{\text{eff}}/\phi_0$, which allows estimation of $R_{\text{eff}} = 550$ nm that gives υ close to integer values [Fig. 3(h)]. The first and most pronounced peak corresponds to a single magnetic flux piercing the area of the ring with an effective radius R_{eff}, and the AB period 4.35 mT. The further peaks represent the higher harmonics at multiples of magnetic flux through the ring area, as the carrier paths encircling the ring multiple times in the clockwise or anticlockwise direction accumulates a phase difference proportional to multiples of ϕ_0. The probability for each subsequent nth round decreases, which leads to the decrease of the overall amplitude of the nth peak. The damping of the peaks amplitude is usually considered as due to phase breaking [56], however the present results are obtained in a fully coherent calculation. Thus we conclude that the decrease of amplitude of higher peaks is due to the carrier wave function leaving the ring in parts in each subsequent round.

VIII. ANTI-KLEIN TO KLEIN TUNNELING

The last experiment we revisit is the transition from anti-Klein tunneling to Klein tunneling in BLG [22] revealed by a dual-gated device with a thin top gate (≈ 150 nm) and a global back gate, the combination of which can form a Fabry-Pérot cavity when tuned into p-n-p or n-p-n junctions. By applying a weak magnetic field, whether the resulting Fabry-Perot interference shows a phase jump or not depends on whether the Fermi energy is close to or away from the band gap. The former corresponds to Berry phase close to π, leading to Klein-like tunneling, and the latter to Berry phase close to 2π, leading to anti-Klein-like tunneling. This experimental observation was well reproduced by transport simulations based on the atomistic TBM scaled by $s_f = 4$ also reported in Ref. [22], for which we apply our effective model of various a based on the same technique of periodic boundary hopping [57–59]. For simplicity, we present the normalized conductance calculated as $g = (e^2/h) \int_{-k_F}^{k_F} T(k_y)dk_y$, where k_F is the Fermi momentum and the angle-resolved transmission function $T(k_y)$ takes the carrier-density profile $n(x) = (V_{\text{TG}}C_{\text{TG}} + V_{\text{BG}}C_{\text{BG}} + V_c C_c)/e$ along the system as the main input. We follow all details of the capacitance for the bottom gate $C_{\text{BG}}(x)$, top gate $C_{\text{TG}}(x)$, and contacts $C_c(x)$ obtained
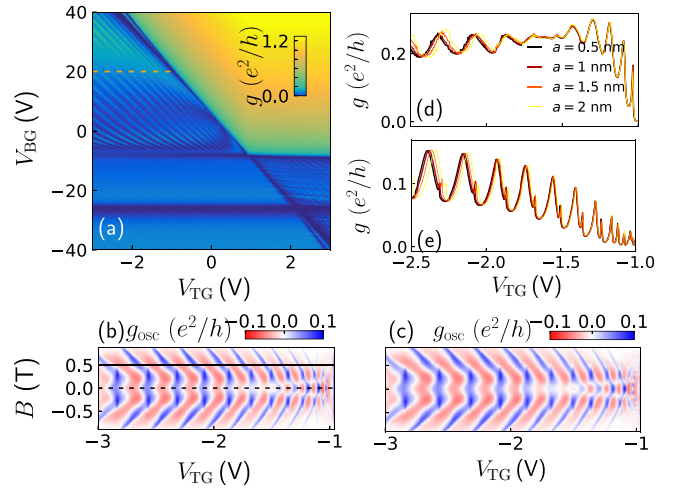

FIG. 4. (a) Normalized conductance g of a dual-gated BLG device as a function of V_{TG} and V_{BG} at zero magnetic field obtained within the effective model with $a = 1$ nm. The oscillatory part of g as a function of V_{TG} and B with fixed V_{BG} corresponding to the dashed line in (a), based on (b) the effective model and (c) the atomistic TBM. Line cuts along the dashed line ($B = 0$) and solid line ($B = 0.4$ T) on (b) are shown in (d),(e), respectively, using various a.

from the finite-element electrostatic simulation provided in Ref. [22].

Figure 4(a) shows $g(V_{\text{TG}}, V_{\text{BG}})$ with $V_c = 1.1$ V, calculated with the effective four-band model with $a = 1$ nm, agreeing very well with the simulation result of Ref. [22]. Figure 4(b) shows the oscillating part of the normalized conductance, g_{osc}, as a function of V_{TG} and B with fixed $V_{\text{BG}} = 20$ V, calculated using the effective model with $a = 0.5$ nm. Compared to Fig. 4(c) done with the atomistic TBM ($s_f = 1$), the effective model shows stunningly precise performance. We further check the influence of the lattice spacing a. Figures 4(d) and 4(e) show the line cuts of conductance at $B = 0$ and $B = 0.4$ T, respectively, with a varying from 0.5 to 2 nm. When increasing a, the results are consistent at low V_{TG}, but start to deviate slightly when the voltage is far from the charge neutrality point, particularly for the curve with $a = 2$ nm. Overall, the agreement is rather satisfactory.

IX. CONCLUDING REMARKS

The effective model presented here shows its power and precision in capturing features of large-scale two-dimensional transport in Bernal-stacked BLG, and hence brings the community one significant step forward. Further applications of our model can be, for example, BLG superlattices, which have recently been proposed as a medium for flat energy bands [60,61], or other transport experiments, which were beyond the reach of atomistic TBM,

such as quantum point contacts with constriction defined by displacement field [6,7] as well as electrostatic BLG quantum dots [8,12,13,62,63]. Although the discretized continuum Hamiltonian is a simple one with only dimer interlayer hopping, that does not contain the trigonal warping requiring inclusion of the skew interlayer hopping, it is sufficient for basic applications presented in this paper, and generally for the description of phenomena, which probe the energy range beyond the trigonally warped region. The trigonal warping effects can manifest themselves in certain transport experiments [64]. For such specific applications, the skew hopping could be included in the original continuum Hamiltonian (1), which would yield a modified effective model.

Additionally, the discretization scheme used in this work can be used to other Hamiltonians describing other materials, where spatial derivatives are replaced by finite differences. As shown in this work, the effective four-band model accounts for both valleys K and K' from the hexagonal BZ of the original TBM. We expect such mapping to be found in other hexagonal materials, providing a tool for efficient modeling of realistic devices.

ACKNOWLEDGMENTS

APPENDIX A: EFFECTIVE-MODEL BAND STRUCTURE

It is instructive to derive the energy bands within the effective model and see its low-energy properties. For an artificial infinite 2D square lattice, the Hamiltonian can be expressed as

$$H_s = \begin{pmatrix} U/2 & h_{12} & \gamma_1 & 0 \\ h_{21} & U/2 & 0 & 0 \\ \gamma_1 & 0 & -U/2 & h_{34} \\ 0 & 0 & h_{43} & -U/2 \end{pmatrix}, \quad \text{(A1)}$$

where

$$h_{12} = h_{21}^* = \frac{it}{2}(-e^{ik_x a} + e^{-ik_x a}) + \frac{t}{2}(e^{ik_y a} - e^{-ik_y a})$$
$$= t(\sin k_x a + i \sin k_y a), \quad \text{(A2)}$$

and similarly $h_{34} = h_{43}^* = t(\sin k_x a - i \sin k_y a)$. Diagonalizing Eq. (A1), we obtain Eq. (5) in the main text.

APPENDIX B: LOW-k EXPANSION OF THE BAND STRUCTURE

As described in the main text, in the effective model, the number of the K and K' valleys is doubled [Fig. 1(d), upper panel]. However, out of the doubly degenerate cones, those in the middle of the edge of the Brillouin zone, $\mathbf{k} = (\pm\pi/a, 0)$ and $\mathbf{k} = (0, \pm\pi/a)$, exhibit the electronic properties of the K' valley of BLG, while those in the corners of the Brillouin zone – of the K valley. This can be seen for example by substituting $\mathbf{k} = (k_x + \pi/a, k_y)$ in Eq. (A1). Then, the matrix elements become

$$\begin{aligned} h_{12} = h_{21}^* = t(\sin k_x a - i \sin k_y a) &\approx t(k_x a - i k_y a), \\ h_{34} = h_{43}^* = t(\sin k_x a + i \sin k_y a) &\approx t(k_x a + i k_y a), \end{aligned} \quad \text{(B1)}$$

where the last step is the approximate form at low energy. With $t = \hbar v_f / a$, the Hamiltonian matrix is the same as Eq. (1) in the main text, with $\xi = -1$ and $V = 0$. By analogy, at $\mathbf{k} = (k_x + \pi/a, k_y + \pi/a)$, one can arrive at $h_{12} = h_{21}^* = -t(k_x a + i k_y a)$ and $h_{34} = h_{43}^* = -t(k_x a - i k_y a)$, which corresponds to the K-valley Hamiltonian.

APPENDIX C: BAND OFFSET AND ASYMMETRY PARAMETER

Considering the parallel-plate capacitor model, we obtain the carrier density

$$n(x,y) = \frac{C_{\text{BG}}V_{\text{BG}} + C_{\text{ring}}(x,y)V_{\text{ring}} + C_{\text{TG}}(x,y)V_{\text{TG}}}{e}$$

in the device. For a given value of n at the point (x,y), we calculate the asymmetry parameter U as described in the Supplemental Material of Ref. [21].

Given the carrier density n and U, one can obtain the band offset from Eq. (5). For this, we notice that the energy dispersion is to a good approximation isotropic at $|E| \lesssim 1$ eV, an energy range well suited for the quantum transport calculations. Equation (5) can be simplified by considering the direction along $k_y = 0$, and substituting $(\sin^2 k_x a + \sin^2 k_y a)$ for $\sin^2 k_x a$. Then, the asymmetry parameter is obtained by replacing k_x by $\sqrt{\pi |n|}$ and adding a minus sign

$$V = -\text{sgn}(n)\left(t^2 \sin^2(\sqrt{\pi n}a) + \frac{U^2}{4} + \frac{\gamma_1^2}{2} - \frac{1}{2}\left[\gamma_1^4 + 4t^2 \sin^2(\sqrt{\pi n}a)(U^2 + \gamma_1^2)\right]^{1/2}\right)^{1/2}. \tag{C1}$$

Both V and U are further used in the effective Hamiltonian onsite energy.

APPENDIX D: GATE-INDUCED AHARANOV-BOHM RING

1. Model functions for the gate capacitance

As described in the main text, the ring-shaped gate is given by a model function $C_{\text{ring}}(x, y) = C_{\text{ring}_0} f(x, y)$, as shown in Fig. 3(c) of the main text, where

$$f(x,y) = 1 - \left\{1 - \left[1 - \frac{1}{4}\left(\tanh\frac{r - R_{\text{out}}}{d_{\text{smooth}}} + 1\right)\left(\tanh\frac{y - w/2}{d_{\text{smooth}}} + \tanh\frac{-y - w/2}{d_{\text{smooth}}} + 2\right)\right]\frac{1}{2}\left(\tanh\frac{r - R_{\text{in}}}{d_{\text{smooth}}} + 1\right)\right\}^{3.5} \tag{D1}$$

and for the top gate, $C_{\text{TG}}(x, y) = C_{\text{TG}_0}(1 - f(x, y))g(x)$, as presented in Fig. 3(b), with

$$g(x) = \left[1 - \frac{1}{3}\left(\tanh\frac{x - L_{\text{TG}}/2}{d_{\text{smooth}}} + \tanh\frac{-x - L_{\text{TG}}/2}{d_{\text{smooth}}} + 2\right)\right]^{20}, \tag{D2}$$

where the multiplication by $g(x)$ is for cropping the top-gate capacitance at $x = \pm L_{\text{TG}}/2$. In Eq. (D1), $r = \sqrt{x^2 + y^2}$, and we assume $C_{\text{ring}_0} = C_{\text{BG}}/0.77$ and $C_{\text{TG}_0} = C_{\text{BG}}/0.99$ in accordance with Ref. [19]. $R_{\text{in}} = 500$ nm and $R_{\text{out}} = 580$ nm are the inner and outer radius of the ring, respectively, $w = 80$ nm is the width of the channel, $L_{\text{TG}} = 1600$ nm is the length of the top gate, and $d_{\text{smooth}} = 40$ nm defines the smoothness.

2. Basic characterization of transport simulations

We consider a system connected to two contacts simulated as semi-infinite leads. In the system described above, it is possible to tune independently the densities and band gaps in the region under the ring-shaped gate and the region beyond it but covered by the top gate (referred to as bulk from now on). To form a ring, BLG in the ring region is tuned to a nonzero density while the bulk should be set within the band gap. To find the conditions in which these requirements are satisfied, we first calculate the inverse transmission $1/T$ at zero magnetic field with either $V_{\text{ring}} = 0$ or $V_{\text{TG}} = 0$, and sweeping the remaining voltages. For the calculation within the effective model we choose zero Fermi energy and lattice spacing $a = 1.5$ nm. Figure 3(d) shows $1/T$ as a function of V_{ring} and V_{BG}, with $V_{\text{TG}} = 0$. The nearly horizontal line of high $1/T$ is the charge neutrality line of the region over the backgate and not covered by the top gate and ring gate. The diagonal line of slightly increased $1/T$ between $(V_{\text{ring}}, V_{\text{BG}}) = (-5\text{ V}, 6\text{ V})$ and $(5\text{ V}, -6\text{ V})$ is the charge neutrality line of the region controlled by the ring gate. Similarly, in Fig. 3(e), the scan of $1/T$ is plotted as a function of V_{TG} and

V_{BG}, with $V_{\text{ring}} = 0$. We observe a similar behavior but with a slightly lower slope of the bulk charge neutrality line from $(V_{\text{TG}}, V_{\text{BG}}) = (-6\text{ V}, 6\text{ V})$ and $(6\text{ V}, -6\text{ V})$. Choosing a combination of $(V_{\text{BG}}, V_{\text{TG}})$ along this charge neutrality line, one can gap out the bulk region, while the ring-shaped area is conducting.

Comparison of $1/T$ calculated here and the two-terminal resistance in Ref. [19] deserves a comment. The diagonal charge neutrality line in the scan of $1/T(V_{\text{ring}}, V_{\text{BG}})$ is less pronounced in the calculations than in the measurement [19] due to the presence of conducting region in the bulk area. Moreover, the experiment [19] showed two horizontal charge neutrality lines, likely caused by nonuniform intrinsic doping in certain regions of the device. The effects of intrinsic doping were neglected here since the main focus of this study is the quantum ring performance. Despite these qualitative differences, the agreement between the $1/T$ maps and the two-terminal resistance in Ref. [19] is good, particularly the positions of the diagonal charge neutrality lines.

APPENDIX E: TRANSPORT CALCULATION

In the main text, calculations for BLG are based on the effective model, as well as the tight-binding model. The tight-binding Hamiltonian can be summarized as

$$H = -\sum_{\langle i,j \rangle} t_{ij} c_i^\dagger c_j + \sum_j \varepsilon(\mathbf{r}_j) c_j^\dagger c_j, \tag{E1}$$

where the first sum runs over nearest neighbors, and the second sum contains the onsite energies, c_i ($c_i^\dagger$) is annihilation (creation) operator of an electron on site i with the

coordinates $\mathbf{r}_i = (x_i, y_i)$, t_{ij} is the nearest-neighbor hopping parameter with $t_{ij} = t_0 = 3$ eV, and ε is the on-site energy. In addition, we adopt the scalable tight-binding model [23], where the hopping parameter is scaled as $t' = t_0/s_f$ and the lattice spacing $a' = a_0 s_f$, s_f is the scaling factor, and we use $a = 0.142$ nm. In BLG, in addition to the intralayer t_0, the interlayer hoppings between the dimer sites are included, with $t_{ij} = \gamma_1 = 0.39$ eV. The external magnetic field $\mathbf{B} = (0, 0, B)$ is introduced by including the Peierls phase in the hopping integrals, $t_{ij} \rightarrow t_{ij} e^{i\phi}$, with $\phi = -\frac{e}{\hbar} \int_{\mathbf{r}_i}^{\mathbf{r}_j} \mathbf{A} \cdot d\mathbf{r}$, where the integration runs from the site at $\mathbf{r}_i$ to the site at $\mathbf{r}_j$, and the vector potential $\mathbf{A}$ satisfies $\nabla \times \mathbf{A} = \mathbf{B}$. In the effective model, the magnetic field is also introduced via the Peierls substitution $t \rightarrow t e^{i\phi}$. The transport calculation is performed using the Kwant package [65] for the nanoring, and the wave-function matching method [66] for the other systems.

APPENDIX F: SPEEDUP

In Fig. 2, we have shown that the ribbon band structures based on the effective model agree well with those based on the lattice model (along the armchair direction), with and without magnetic field, within a reasonable range of energy. The consistency was clearly visible, but not the reduction in computation time. Figure 5 shows the computation time as a function of the lattice spacing a for the ribbon band structure based on the effective model. The width of the ribbon $W = 201$ nm and the number of k points $N_k = 201$ are fixed for all data points. The computation time within the shown range is approximately 2 orders of magnitude shorter than that based on the $s_f = 4$ lattice model (about 492 s). For the $s_f = 1$ lattice model, computing all eigenenergies will take nearly 8 h. All tests for the computation time shown here were done on a laptop equipped with processor 13th Gen Intel(R) Core(TM) i5-1335U 1.30 GHz and 16.0 GB of memory.

As a side note, for the integer quantum Hall calculation within the effective model, we estimated the computational gain with respect to the atomistic TBM. In the scalable TBM with $s_f = 2$, the number of sites is about 3.7 million, compared to the 200 thousand needed for the effective model. Including the four bands, the total size of the problem is 800 thousand, which is a much more reasonable number for numerical calculations. This, in addition to the speed-up plot of Fig. 5, proves the advantage of the effective model.

APPENDIX G: DENSITY LIMITS AND INCLUDING DEFECTS

We estimate the upper limits of density that can be accurately described by the effective model. The effective model energy [Eq. (5) of the main text] converges to the result of the continuum model when $ka \ll 1$. We
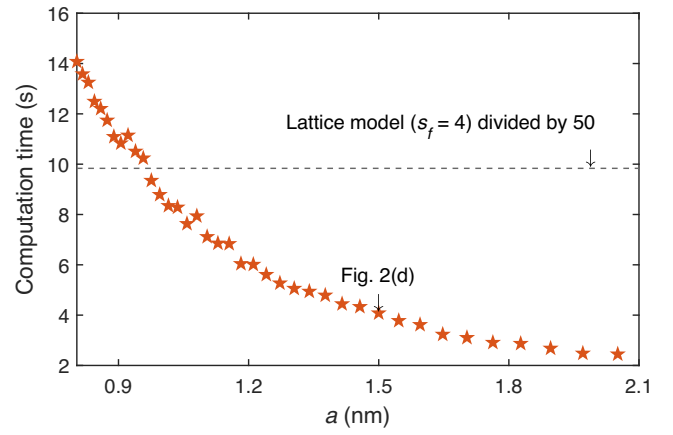

FIG. 5. Computation time of the band structure for a 201-nm-wide BLG ribbon based on the effective model, as a function of lattice spacing a.

estimated that it can describe the band structure well when $ka < 0.3$. Plugging in the relation $k = \sqrt{\pi n}$, where n is the carrier density, we can estimate the carrier density range for a given lattice spacing a as $n < (1/\pi)(0.3/a)^2$. As an illustrative example, we may consider a reasonably small lattice spacing to be about $a = 0.5$ nm, which assures high accuracy and relatively good performance. Then, the maximum density available for accurate calculations is $n_{\max} = (1/\pi)(0.3/a)^2 \approx 11.46 \times 10^{16}$ m^{-2}. A typical density value in experimental samples is of that order of magnitude.

The model can include disorder and defects similarly as the traditional tight binding model, for example, by simulating disorder with Gaussian-type random potential or Anderson type of disorder as random onsite energy. One needs to keep in mind that the effect of disorder may not be exactly the same in the effective model and the tight binding model, and will also vary depending on the grid spacing a used. In other words, the random onsite energy magnitude in different models will lead to different mean free paths. Quantification of this effect is beyond the scope of this work. Similar comment concerns the defects: a site of the square lattice can be removed to simulate defects, and the overall effect may differ between the tight binding model and the square lattice model with various a.

[1] Y. Cao, V. Fatemi, S. Fang, K. Watanabe, T. Taniguchi, E. Kaxiras, and P. Jarillo-Herrero, Unconventional superconductivity in magic-angle graphene superlattices, Nature **556**, 43 (2018).

[2] H. Zhou, L. Holleis, Y. Saito, L. Cohen, W. Huynh, C. L. Patterson, F. Yang, T. Taniguchi, K. Watanabe, and A. F. Young, Isospin magnetism and spin-polarized superconductivity in Bernal bilayer graphene, Science **375**, 774 (2022).

[3] Z. Zheng, Q. Ma, Z. Bi, S. de la Barrera, M.-H. Liu, N. Mao, Y. Zhang, N. Kiper, K. Watanabe, T. Taniguchi, J. Kong, W. A. Tisdale, R. Ashoori, N. Gedik, L. Fu, S.-Y. Xu, and P. Jarillo-Herrero, Unconventional ferroelectricity in moiré heterostructures, Nature **588,** 71 (2020).

[4] Y.-C. Tsui, M. He, Y. Hu, E. Lake, T. Wang, K. Watanabe, T. Taniguchi, M. P. Zaletel, and A. Yazdani, Direct observation of a magnetic-field-induced Wigner crystal, Nature **628,** 287 (2024).

[5] H. Overweg, H. Eggimann, X. Chen, S. Slizovskiy, M. Eich, R. Pisoni, Y. Lee, P. Rickhaus, K. Watanabe, T. Taniguchi, V. Fal'ko, T. Ihn, and K. Ensslin, Electrostatically induced quantum point contacts in bilayer graphene, Nano Lett. **18,** 553 (2018).

[6] R. Kraft, I. V. Krainov, V. Gall, A. P. Dmitriev, R. Krupke, I. V. Gornyi, and R. Danneau, Valley subband splitting in bilayer graphene quantum point contacts, Phys. Rev. Lett. **121,** 257703 (2018).

[7] H. Overweg, A. Knothe, T. Fabian, L. Linhart, P. Rickhaus, L. Wernli, K. Watanabe, T. Taniguchi, D. Sánchez, J. Burgdörfer, F. Libisch, V. I. Fal'ko, K. Ensslin, and T. Ihn, Topologically nontrivial valley states in bilayer graphene quantum point contacts, Phys. Rev. Lett. **121,** 257702 (2018).

[8] L. Banszerus, S. Möller, E. Icking, K. Watanabe, T. Taniguchi, C. Volk, and C. Stampfer, Single-electron double quantum dots in bilayer graphene, Nano Lett. **20,** 2005 (2020).

[9] Y. Lee, A. Knothe, H. Overweg, M. Eich, C. Gold, A. Kurzmann, V. Klasovika, T. Taniguchi, K. Wantanabe, V. Fal'ko, T. Ihn, K. Ensslin, and P. Rickhaus, Tunable valley splitting due to topological orbital magnetic moment in bilayer graphene quantum point contacts, Phys. Rev. Lett. **124,** 126802 (2020).

[10] M. T. Allen, J. Martin, and A. Yacoby, Gate-defined quantum confinement in suspended bilayer graphene, Nat. Commun. **3,** 934 (2012).

[11] A. S. M. Goossens, S. C. M. Driessen, T. A. Baart, K. Watanabe, T. Taniguchi, and L. M. K. Vandersypen, Gate-defined confinement in bilayer graphene-hexagonal boron nitride hybrid devices, Nano Lett. **12,** 4656 (2012).

[12] M. Eich, F. c. v. Herman, R. Pisoni, H. Overweg, A. Kurzmann, Y. Lee, P. Rickhaus, K. Watanabe, T. Taniguchi, M. Sigrist, T. Ihn, and K. Ensslin, Spin and valley states in gate-defined bilayer graphene quantum dots, Phys. Rev. X **8,** 031023 (2018).

[13] A. Kurzmann, H. Overweg, M. Eich, A. Pally, P. Rickhaus, R. Pisoni, Y. Lee, K. Watanabe, T. Taniguchi, T. Ihn, and K. Ensslin, Charge detection in gate-defined bilayer graphene quantum dots, Nano Lett. **19,** 5216 (2019).

[14] L. Seemann, A. Knothe, and M. Hentschel, Gate-tunable regular and chaotic electron dynamics in ballistic bilayer graphene cavities, Phys. Rev. B **107,** 205404 (2023).

[15] I. Martin, Y. M. Blanter, and A. F. Morpurgo, Topological confinement in bilayer graphene, Phys. Rev. Lett. **100,** 036804 (2008).

[16] P. San-Jose, E. Prada, E. McCann, and H. Schomerus, Pseudospin valve in bilayer graphene: Towards graphene-based pseudospintronics, Phys. Rev. Lett. **102,** 247204 (2009).

[17] J. Li, K. Wang, K. J. McFaul, Z. Zern, Y. Ren, K. Watanabe, T. Taniguchi, Z. Qiao, and J. Zhu, Gate-controlled topological conducting channels in bilayer graphene, Nat. Nanotechnol. **11,** 1060 (2016).

[18] J. Ingla-Aynés, A. L. R. Manesco, T. S. Ghiasi, S. Volosheniuk, K. Watanabe, T. Taniguchi, and H. S. J. van der Zant, Specular electron focusing between gate-defined quantum point contacts in bilayer graphene, Nano Lett. **23,** 5453 (2023).

[19] S. Iwakiri, F. K. de Vries, E. Portolés, G. Zheng, T. Taniguchi, K. Watanabe, T. Ihn, and K. Ensslin, Gate-defined electron interferometer in bilayer graphene, Nano Lett. **22,** 6292 (2022).

[20] H. Fu, K. Huang, K. Watanabe, T. Taniguchi, M. Kayyalha, and J. Zhu, Aharonov–Bohm oscillations in bilayer graphene quantum Hall edge state Fabry–Pérot interferometers, Nano Lett. **23,** 718 (2023).

[21] A. Varlet, M.-H. Liu, V. Krueckl, D. Bischoff, P. Simonet, K. Watanabe, T. Taniguchi, K. Richter, K. Ensslin, and T. Ihn, Fabry-Pérot interference in gapped bilayer graphene with broken anti-Klein tunneling, Phys. Rev. Lett. **113,** 116601 (2014).

[22] R. Du, M.-H. Liu, J. Mohrmann, F. Wu, R. Krupke, H. von Löhneysen, K. Richter, and R. Danneau, Tuning anti-Klein to Klein tunneling in bilayer graphene, Phys. Rev. Lett. **121,** 127706 (2018).

[23] M.-H. Liu, P. Rickhaus, P. Makk, E. Tóvári, R. Maurand, F. Tkatschenko, M. Weiss, C. Schönenberger, and K. Richter, Scalable tight-binding model for graphene, Phys. Rev. Lett. **114,** 036601 (2015).

[24] D. B. Kaplan, A method for simulating chiral fermions on the lattice, Phys. Lett. B **288,** 342 (1992).

[25] S. D. Drell, M. Weinstein, and S. Yankielowicz, Strong-coupling field theories. II. Fermions and gauge fields on a lattice, Phys. Rev. D **14,** 1627 (1976).

[26] K. G. Wilson, in *13th International School of Subnuclear Physics: New Phenomena in Subnuclear Physics* (New York, 1975).

[27] L. Susskind, Lattice fermions, Phys. Rev. D **16,** 3031 (1977).

[28] R. Stacey, Eliminating lattice fermion doubling, Phys. Rev. D **26,** 468 (1982).

[29] J. B. Kogut, The lattice gauge theory approach to quantum chromodynamics, Rev. Mod. Phys. **55,** 775 (1983).

[30] C. W. J. Beenakker, A. Donís Vela, G. Lemut, M. J. Pacholski, and J. Tworzydło, Tangent fermions: Dirac or Majorana fermions on a lattice without fermion doubling, Ann. Phys. **535,** 2300081 (2023).

[31] J. Tworzydło, C. W. Groth, and C. W. J. Beenakker, Finite difference method for transport properties of massless Dirac fermions, Phys. Rev. B **78,** 235438 (2008).

[32] A. R. Hernández and C. H. Lewenkopf, Finite-difference method for transport of two-dimensional massless Dirac fermions in a ribbon geometry, Phys. Rev. B **86,** 155439 (2012).

[33] K. M. M. Habib, R. N. Sajjad, and A. W. Ghosh, Modified Dirac Hamiltonian for efficient quantum mechanical simulations of micron sized devices, Appl. Phys. Lett. **108,** 113105 (2016).

[34] B. Szafran, A. Mreńca-Kolasińska, and D. Żebrowski, Finite-difference method for Dirac electrons in circular quantum dots, Phys. Rev. B **99,** 195406 (2019).

[35] A. Ziesen, I. C. Fulga, and F. Hassler, Geometry-independent tight-binding method for massless Dirac fermions in two dimensions, Phys. Rev. B **107,** 195409 (2023).

[36] D. P. Żebrowski, F. M. Peeters, and B. Szafran, Double quantum dots defined in bilayer graphene, Phys. Rev. B **96,** 035434 (2017).

[37] K. S. Novoselov, A. K. Geim, S. V. Morozov, D. Jiang, M. I. Katsnelson, I. V. Grigorieva, S. V. Dubonos, and A. A. Firsov, Two-dimensional gas of massless Dirac fermions in graphene, Nature **438,** 197 (2005).

[38] Y. Zhang, Y.-W. Tan, H. L. Stormer, and P. Kim, Experimental observation of the quantum Hall effect and Berry's phase in graphene, Nature **438,** 201 (2005).

[39] T. Taychatanapat, K. Watanabe, T. Taniguchi, and P. Jarillo-Herrero, Electrically tunable transverse magnetic focusing in graphene, Nat. Phys. **9,** 225 (2013).

[40] E. McCann and M. Koshino, The electronic properties of bilayer graphene, Rep. Prog. Phys. **76,** 056503 (2013).

[41] S. Datta, *Electronic Transport in Mesoscopic Systems* (Cambridge University Press, Cambridge, 1995).

[42] H. U. Baranger and A. D. Stone, Electrical linear-response theory in an arbitrary magnetic field: A new Fermi-surface formation, Phys. Rev. B **40,** 8169 (1989).

[43] A. Mreńca-Kolasińska, S.-C. Chen, and M.-H. Liu, Probing miniband structure and Hofstadter butterfly in gated graphene superlattices via magnetotransport, npj 2D Mater. Appl. **7,** 64 (2023).

[44] Y. Aharonov and D. Bohm, Significance of electromagnetic potentials in the quantum theory, Phys. Rev. **115,** 485 (1959).

[45] P. Recher, B. Trauzettel, A. Rycerz, Y. M. Blanter, C. W. J. Beenakker, and A. F. Morpurgo, Aharonov-Bohm effect and broken valley degeneracy in graphene rings, Phys. Rev. B **76,** 235404 (2007).

[46] J. Wurm, M. Wimmer, H. U. Baranger, and K. Richter, Graphene rings in magnetic fields: Aharonov–Bohm effect and valley splitting, Semicond. Sci. Tech. **25,** 034003 (2010).

[47] A. Mreńca-Kolasińska and B. Szafran, Lorentz force effects for graphene Aharonov-Bohm interferometers, Phys. Rev. B **94,** 195315 (2016).

[48] S. Russo, J. B. Oostinga, D. Wehenkel, H. B. Heersche, S. S. Sobhani, L. M. K. Vandersypen, and A. F. Morpurgo, Observation of Aharonov-Bohm conductance oscillations in a graphene ring, Phys. Rev. B **77,** 085413 (2008).

[49] M. Huefner, F. Molitor, A. Jacobsen, A. Pioda, C. Stampfer, K. Ensslin, and T. Ihn, The Aharonov–Bohm effect in a side-gated graphene ring, New J. Phys. **12,** 043054 (2010).

[50] D. Smirnov, H. Schmidt, and R. J. Haug, Aharonov-Bohm effect in an electron-hole graphene ring system, Appl. Phys. Lett. **100,** 203114 (2012).

[51] D. Smirnov, J. C. Rode, and R. J. Haug, Suppression of decoherence in a graphene monolayer ring, Appl. Phys. Lett. **105,** 082112 (2014).

[52] J. Dauber, M. Oellers, F. Venn, A. Epping, K. Watanabe, T. Taniguchi, F. Hassler, and C. Stampfer, Aharonov-Bohm oscillations and magnetic focusing in ballistic graphene rings, Phys. Rev. B **96,** 205407 (2017).

[53] Y. Ronen, T. Werkmeister, D. Haie Najafabadi, A. T. Pierce, L. E. Anderson, Y. J. Shin, S. Y. Lee, Y. H. Lee, B. Johnson, K. Watanabe, T. Taniguchi, A. Yacoby, and P. Kim, Aharonov–Bohm effect in graphene-based Fabry–Pérot quantum Hall interferometers, Nat. Nanotechnol. **16,** 563 (2021).

[54] C. Déprez, L. Veyrat, H. Vignaud, G. Nayak, K. Watanabe, T. Taniguchi, F. Gay, H. Sellier, and B. Sacépé, A tunable Fabry–Pérot quantum Hall interferometer in graphene, Nat. Nanotechnol. **16,** 555 (2021).

[55] S. Iwakiri, A. Mestre-Torà, E. Portolés, M. Visscher, M. Perego, G. Zheng, T. Taniguchi, K. Watanabe, M. Sigrist, T. Ihn, and K. Ensslin, Tunable quantum interferometer for correlated moiré electrons, Nat. Commun. **15,** 390 (2024).

[56] A. E. Hansen, A. Kristensen, S. Pedersen, C. B. Sørensen, and P. E. Lindelof, Mesoscopic decoherence in Aharonov-Bohm rings, Phys. Rev. B **64,** 045327 (2001).

[57] M. Wimmer, *Quantum transport in nanostructures: From computational concepts to spintronics in graphene and magnetictunnel junctions*, Ph.D. thesis, Universitat Regensburg, 2008.

[58] M.-H. Liu and K. Richter, Efficient quantum transport simulation for bulk graphene heterojunctions, Phys. Rev. B **86,** 115455 (2012).

[59] M.-H. Liu, J. Bundesmann, and K. Richter, Spin-dependent Klein tunneling in graphene: Role of Rashba spin-orbit coupling, Phys. Rev. B **85,** 085406 (2012).

[60] S. A. A. Ghorashi, A. Dunbrack, A. Abouelkomsan, J. Sun, X. Du, and J. Cano, Topological and stacked flat bands in bilayer graphene with a superlattice potential, Phys. Rev. Lett. **130,** 196201 (2023).

[61] J. Sun, S. A. A. Ghorashi, K. Watanabe, T. Taniguchi, F. Camino, J. Cano, and X. Du, Signature of correlated insulator in electric field controlled superlattice, arXiv:2306.06848.

[62] L. Banszerus, B. Frohn, A. Epping, D. Neumaier, K. Watanabe, T. Taniguchi, and C. Stampfer, Gate-defined electron-hole double dots in bilayer graphene, Nano Lett. **18,** 4785 (2018).

[63] L. Banszerus, B. Frohn, T. Fabian, S. Somanchi, A. Epping, M. Müller, D. Neumaier, K. Watanabe, T. Taniguchi, F. Libisch, B. Beschoten, F. Hassler, and C. Stampfer, Observation of the spin-orbit gap in bilayer graphene by one-dimensional ballistic transport, Phys. Rev. Lett. **124,** 177701 (2020).

[64] C. Gold, A. Knothe, A. Kurzmann, A. Garcia-Ruiz, K. Watanabe, T. Taniguchi, V. Fal'ko, K. Ensslin, and T. Ihn, Coherent jetting from a gate-defined channel in bilayer graphene, Phys. Rev. Lett. **127,** 046801 (2021).

[65] C. W. Groth, M. Wimmer, A. R. Akhmerov, and X. Waintal, Kwant: A software package for quantum transport, New J. Phys. **16,** 063065 (2014).

[66] K. Kolasiński, B. Szafran, B. Brun, and H. Sellier, Interference features in scanning gate conductance maps of quantum point contacts with disorder, Phys. Rev. B **94,** 075301 (2016).